Nano Research
2023, 16(5): 8025–8035

ISSN 1998-0124 CN 11-5974/O4
https://doi.org/10.1007/s12274-023-5466-8

Research Article

Super-elastic and mechanically durable MXene-based nanocomposite aerogels enabled by interfacial engineering with dual crosslinking strategy

Yan Sun[1,2], Xin Yang[3], Ruonan Ding[4], Sung Yong Hong[5], Jinwoo Lee[6], Zongfu An[7], Mei Wang[8], Yifei Ma[8], Jae-Do Nam[6,7], and Jonghwan Suhr[6,9] (✉)

[1] *China Copper Institute of Engineering and Technology, Chinalco Research Institute of Science and Technology Co., Ltd., Beijing 102200, China*
[2] *Center for Composite Materials and Concurrent Design, Sungkyunkwan University, Suwon 16419, Republic of Korea*
[3] *Key Laboratory for Light-weight Materials, Nanjing Tech University, Nanjing 210009, China*
[4] *Department of Energy Science, Sungkyunkwan University, Suwon 16419, Republic of Korea*
[5] *MPP PJT. PO R&D Center Polyolefin Business, Petrochemicals Division, LG Chem, Daejeon 34122, Republic of Korea*
[6] *Department of Polymer Science and Engineering, Sungkyunkwan University, Suwon 16419, Republic of Korea*
[7] *School of Chemical Engineering, Sungkyunkwan University, Suwon 16419, Republic of Korea*
[8] *State Key Laboratory of Quantum Optics and Quantum Optics Devices, Institute of Laser Spectroscopy, Collaborative Innovation Center of Extreme Optics, Shanxi University, Taiyuan 030006, China*
[9] *School of Mechanical Engineering, Sungkyunkwan University, Suwon 16419, Republic of Korea*

Received: 28 October 2022 / **Revised:** 19 December 2022 / **Accepted:** 2 January 2023

ABSTRACT

Recently, MXenes have attracted considerable attention owing to their unique physical and chemical properties. Construction of MXenes to three-dimensional (3D) porous aerogel structures can play a critical role in realizing the profound implications of MXenes, especially for environmental remediation. Nevertheless, developing mechanically robust MXene-based aerogels with reversible compressibility under harsh conditions, such as liquid environments, remains challenging due to the insufficient interfacial strength between MXene nanosheets. Herein, 3D porous MXene-based nanocomposite aerogels are developed by dual physical and chemical crosslinking strategy with poly(vinyl alcohol) and formaldehyde in this study. The developed MXene-based nanocomposite aerogels with designed interfacial engineering exhibit outstanding structural stability and extremely high reversible compressibility up to 98% strain as well as unprecedented mechanical durability (2000 cycles at 50% strain) in water environment. Moreover, the aerogels show adaptable compressibility when exposed to different solvents, which is explained with the Hansen solubility parameter. Thanks to their high compressibility in water, the robust MXene-based aerogels exhibit excellent methylene blue adsorption performance (adsorption capacity of 117.87 $mg \cdot g^{-1}$) and superior recycling efficiency (89.48% at the 3rd cycle). The porous MXene-based nanocomposite aerogels are also demonstrated with outstanding thermal insulation capability. Therefore, by synergistically taking their porous structure and super elasticity in liquid environment, the MXene-based aerogels show great promise in diverse applications including adsorption and separation, wastewater purification desalination, and thermal management.

KEYWORDS

MXenes-based nanocomposite aerogels, dual crosslinking strategy, reversible compressibility, methylene blue adsorption, thermal insulation

1 Introduction

As a new large family of two-dimensional (2D) materials, transition metal carbides and/or nitrides (MXenes), have garnered tremendous research interest since the discovery of $Ti_3C_2T_x$ in 2011 [1, 2]. The structural formula of MXene is $M_{n+1}X_nT_z$, where M refers to the early transition metal, X is carbon and/or nitrogen, T represents surface functional groups such as hydroxyl, oxygen, or fluorine generated during the etching process, and n is an integer between 1 and 3. The surface functional groups render MXene with hydrophilicity and high surface charge (negative zeta potential exceeding −30 mV), ensuring the easy and stable dispersion of MXene in water [3]. These surface functional groups also allow MXene to be readily functionalized with various materials through covalent bonds, hydrogen bonds, or electrostatic interactions [4]. Meanwhile, the transition metal carbide core shows metallic conductivity, enabling fast electron transportation [5, 6]. Therefore, these unique physical and chemical properties of MXene make them extremely attractive with great promise for diverse applications, including energy storage devices [7], electromagnetic interference (EMI) shielding [8], adsorption and separation [9], and therapeutic and biosensing applications [10].

Address correspondence to suhr@skku.edu

Despite their great potential, it remains a challenge to achieve the intended applications of MXene-based materials with high performance due to the aggregation and restacking of MXene nanosheets with strong van der Waals interactions and hydrogen bonds. Macroscopic three-dimensional (3D) porous structures constructed from 2D nanosheets have attracted considerable attention and are expected to play a crucial role in the commercialization and practical applications of 2D materials [1]. Generally, the large specific surface area of 2D nanosheets can be maintained in the 3D porous aerogels as the restacking of nanosheets is effectively inhibited [11]. In addition, 3D porous structures can enhance the accessibility of active sites and transport properties of reaction-relevant species within the entire materials [12]. Therefore, the construction of 3D MXene-based porous aerogels could be an effective strategy to reduce layer aggregation, preserve the large specific surface area, and effective mass transportation, showing great promise for wastewater treatment application. However, it is difficult to obtain mechanically robust MXene aerogels to conquer the harsh application conditions, such as in liquid environments, owing to their weak interfacial strength [13]. To the best of our knowledge, MXene-based aerogels with structural stability and reversible compressibility in liquid environments have not yet been reported. Therefore, although it is of great interest, various issues need to be addressed to develop the mechanically robust MXene-based porous aerogels applicable in liquid environments, such as wastewater treatment application.

To overcome the insufficient mechanical properties of 2D material-based 3D porous structures, a novel dual crosslinking mechanism has been developed in our previous study [14]. Compared to the single crosslinking mechanism, the dual crosslinking mechanism proved to be an effective strategy to adjust the crosslinking density, intensify interfacial strength, and eventually increase structural stability of the 3D porous structures in liquid. In this study, MXene-based 3D porous nanocomposite aerogels were developed by applying the dual physical and chemical crosslinking strategy using poly(vinyl alcohol) (PVA) and formaldehyde. Through the designed interfacial engineering among the functional groups of MXene, PVA, and formaldehyde, the MXene-based nanocomposite (MXene-PVA-formaldehyde (MPF)) aerogels exhibit superior structural stability in water and extremely high compressibility even up to 98% compressive strain, surpassing that of MXene-PVA (MP) aerogels by single crosslinking reaction. More impressively, the MPF aerogels exhibit unprecedented mechanical durability by showing reversible compressibility for more than 2000 cycles under 50% strain. In addition to water, MPF aerogels also show reversible compressibility in organic liquids, including dimethyl sulfoxide (DMSO) and N,N-dimethylformamide (DMF). Considering the negative zeta potential of MXene and the high compressibility of the nanocomposite aerogels in water, the porous MPF aerogels show great potential as effective adsorbents for wastewater treatment application. Taking as one example, the adsorption of methylene blue by MPF aerogels was investigated in this study. It is experimentally observed that the dual-crosslinked MPF aerogels show simultaneously high adsorption capacity and excellent recyclability compared to other MXene-based adsorbents for methylene blue. Finally, the porous MPF aerogels are also demonstrated with outstanding thermal insulation capability.

Therefore, the dual crosslinking mechanism is proven as a successful strategy to prepare MXene-based 3D porous structures with significantly enhanced mechanical properties. In addition to dye adsorption and thermal insulation, MPF aerogels also show great potential in a wide range of applications, including heavy metal removal, desalination, catalysis, and degradation, by taking advantage of their porous structure and high compressibility in various liquid environments.

2 Experimental

Preparation of MXene-based nanocomposite aerogels First, $Ti_3C_2T_x$ MXene was synthesized using the minimally intensive layer delamination (MILD) method as described in the previous work [8]. After intercalation and centrifugation, a small amount of water was added into the sediment to redisperse the multilayer MXene followed by sonication in an ice bath for 30 min under Ar gas protection. Finally, the delaminated few-layer MXene dispersion with a concentration of around 17 mg·mL^{-1} was collected after centrifugation at 3500 rpm for 30 min.

MPF aerogels were synthesized using MXene, PVA, and formaldehyde by the dual crosslinking mechanism. Specifically, 36 mL of MXene dispersion was mixed with 3.6 g of PVA solution (10 wt.%) dropwise under vigorous stirring at room temperature (~ 22 °C). The mixture was then bath-sonicated for 30 min under Ar protection, followed by stirring at room temperature for another 30 min to obtain the MP dispersion. To further prepare the MPF dispersion, 610 μL formaldehyde solution (37 wt.%) was added into MP dispersion at 68 wt.% of PVA and stirred for another 30 min. To accelerate the chemical crosslinking reaction, 33 μL of HCl (35 wt.%–37 wt.%) was added as the catalyst. Finally, MP and MPF aerogels were obtained after heating MP and MPF dispersions in an oven at 40 °C for 20 h, followed by freeze-drying at −80 °C for 48 h. For comparison, freeze-dried MXene (without crosslinking) and PVA-formaldehyde (PF) aerogels (without MXene) were also prepared by freeze-drying at −80 °C for 48 h. It is worth noting here that the mass ratio between MXene and PVA-formaldehyde of MPF aerogel was equal to 1, which was the optimal mass ratio for preparation of the aerogels verified by the experiment. More details about MPF aerogels prepared with other mass ratios are shown in Electronic Supplementary Material (ESM).

3 Results and discussion

3.1 Chemical mechanism

The chemical mechanism for the synthesis of MP aerogels by single crosslinking and MPF aerogels by dual crosslinking strategy is shown in Fig. 1. First, MXene is prepared by the MILD method (Fig. S1 in the ESM). The thickness of MXene nanosheets is around 3 nm, indicating the double-layer structure of the nanosheets synthesized in this study [8]. To prepare MP aerogels, MXene nanosheets are firstly mixed with PVA polymer chains. The surface functional groups, including –OH, –O, and –F, on MXene nanosheets would form hydrogen bonds (physical crosslinking) with the –OH groups on PVA molecules, resulting in weak interaction and insufficient interfacial strength between MXene nanosheets and PVA polymer chains. For MPF aerogels prepared by dual crosslinking reaction, in addition to the hydrogen bonds (physical crosslinking) between MXene and PVA, –OH groups on PVA molecules and –OH groups on MXene nanosheets would further react with –CHO groups from formaldehyde molecules by the acetalization reaction (chemical crosslinking) after adding formaldehyde, which can form new covalent linkage as ether bonds to further bridge MXene nanosheets and PVA polymer chains, leading to the strong interfacial strength between MXene and PVA [15]. Therefore, MPF aerogels consolidated by the dual physical and chemical crosslinking reactions can be guaranteed with significantly enhanced structural stability and mechanical properties, compared

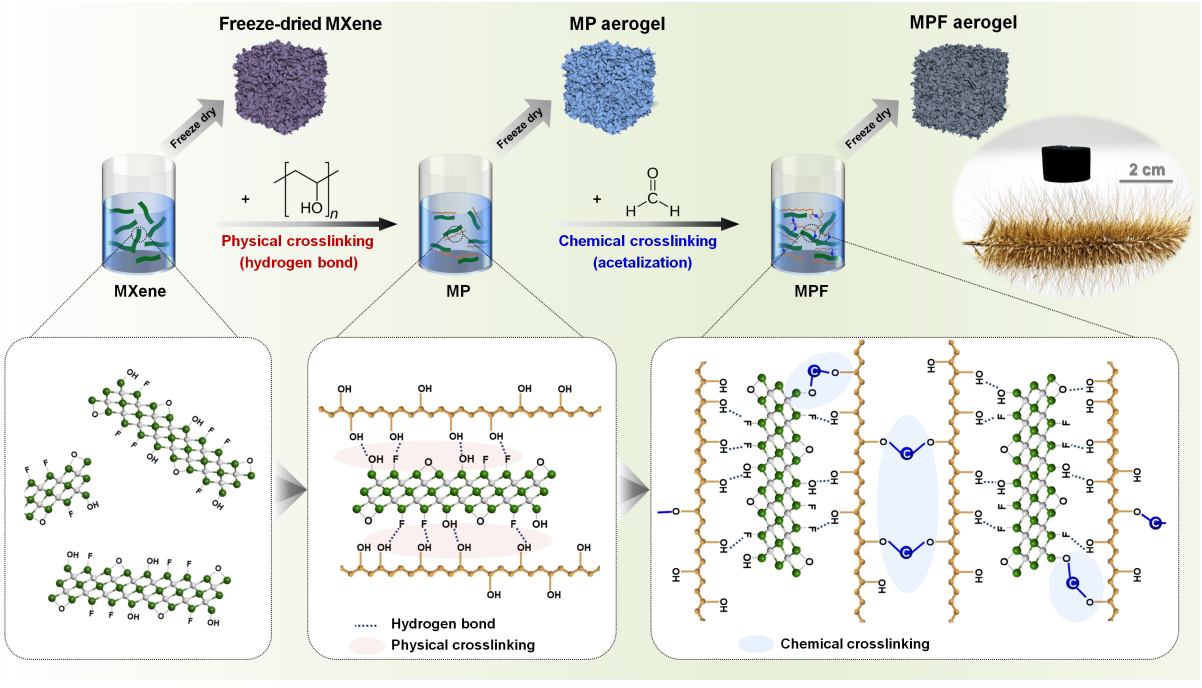

Figure 1 Schematic illustration of the chemical mechanism for synthesizing MP aerogels by the single crosslinking reaction and MPF aerogels by the dual crosslinking reaction.

with MP aerogels by the single physical crosslinking reaction or freeze-dried MXene without crosslinking.

3.2 Structural characterization

Photographic and scanning electron microscopy (SEM) images are shown in Fig. S2 in the ESM and Fig. 2 to demonstrate the morphologies of freeze-dried MXene, MP, and MPF aerogels. The color of freeze-dried MXene is dark purple, while MP aerogel appears in dark blue and MPF aerogel in black color. For internal microstructure, the freeze-dried MXene is observed to be a fragile accumulation of MXene nanosheets with random orientations (Fig. 2(a)), which is easily decomposed into powder under compression. MP aerogels (Fig. 2(b)) have a cellular structure, the pore size is widely ranged from several micrometers to 100 μm. Compared with MP aerogels, MPF aerogels exhibit more uniform pore size distribution with an average pore size value around 70 μm (Fig. 2(c)).

After checking the microstructures, thermogravimetric analysis (TGA) was conducted for MXene, MP aerogels, MPF aerogels, and PVA from 20 to 800 °C under N_2 atmosphere (Fig. 3(a) and Table S1 in the ESM). The weight loss of the materials can be divided into three regions. The first region (100 to around 200 °C) is caused by the evaporation of absorbed water molecules. The second region (230 to 360 °C) can be attributed to the removal of functional groups from MXene sheets and –OH groups from PVA polymers. The third weight loss (360 to 490 °C) could be related to the decomposition of the remaining carbides [15]. The on-set temperature ($T_{on\text{-}set}$) and the temperature at 5% weight loss ($T_{5\%}$) are observed to increase from 247.1 and 268.7 °C for MP aerogel to 265.7 and 279.0 °C for MPF aerogels, respectively. This indicates the increased thermal stability of MPF aerogel with the dual crosslinking mechanism compared to that of MP aerogel with the single crosslinking mechanism.

The difference between MP and MPF aerogels was further verified by X-ray diffraction (XRD) analysis (Fig. 3(b)). The XRD patterns indicate the amorphous structure of PVA based on the broad and weak peak at around 20°. For MXene-based aerogels, the (002) peak is left-shifted gradually from 6.88° for freeze-dried MXene to 6.14° for MP aerogels and finally to 5.34° for MPF

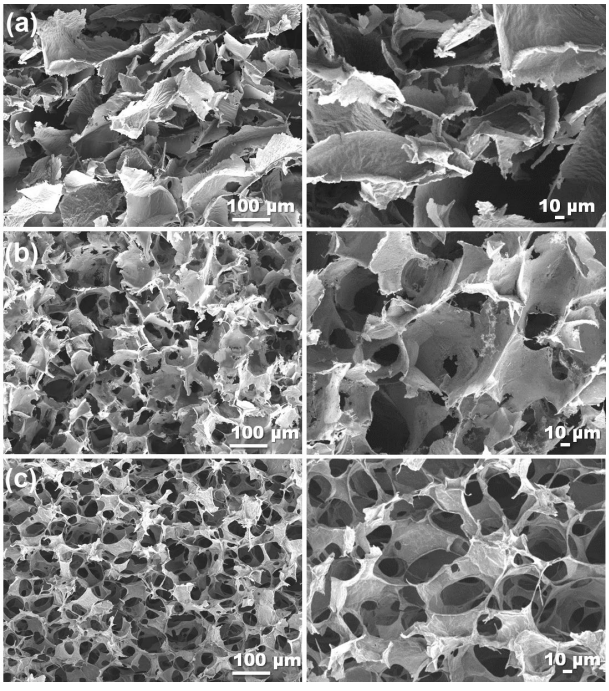

Figure 2 SEM images of (a) freeze-dried MXene, (b) MP aerogels, and (c) MPF aerogels, respectively.

aerogels. This shift can be explained by the increase in the interlayer distance of MXene nanosheets due to the intercalation of PVA polymers after the physical crosslinking reaction. The distance was further increased after the incorporation of formaldehyde molecules into the network by the chemical crosslinking reaction [16]. In addition to the left-shift of peak positions, the intensities of the peaks also decrease from freeze-dried MXene solution to MPF aerogels.

Fourier transform infrared (FTIR) spectra of MXene-based nanocomposite aerogels and PVA are shown in Fig. 3(c). Freeze-dried MXene is characterized with absorption bands located at 3691, 1245, 1078, and 686 cm^{-1}, corresponding to the O–H, C–F, C–O, and Ti–O bonds, respectively [17, 18]. For PVA polymer,

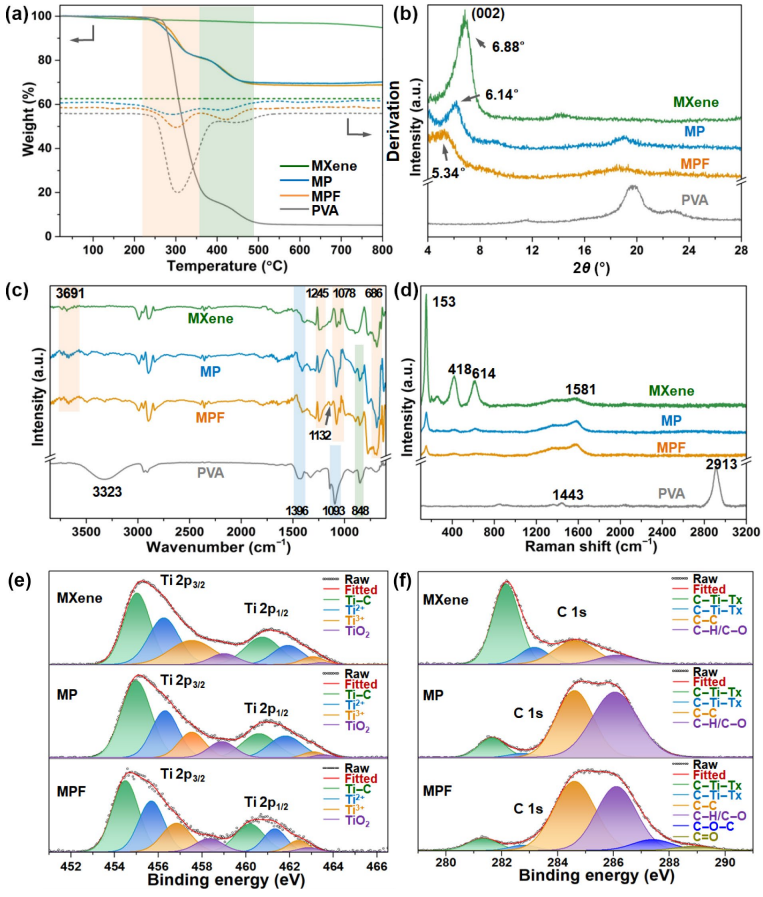

Figure 3 Characterizations of freeze-dried MXene, MP aerogels, and MPF aerogels. (a) Thermogravimetric analysis, (b) XRD patterns, (c) FTIR spectra, and (d) Raman spectra of freeze-dried MXene, MP aerogels, MPF aerogels, and PVA, respectively. High-resolution X-ray photoelectron spectroscopy (XPS) spectra of (e) Ti 2p and (f) C 1s with the deconvoluted results of freeze-dried MXene, MP aerogels, and MPF aerogels, respectively.

the characteristic absorption peaks at 3323, 1396, 1093, and 848 cm^{-1} can be assigned to the O–H stretching, O–H bending, C–O stretching, and C–H bending, respectively [19]. The absorption band of C–H bending can also be observed in MP and MPF aerogels, demonstrating the effective introduction of PVA polymer after the physical crosslinking reaction. Compared to MP aerogel, a new absorption band at 1132 cm^{-1} is observed for MPF aerogel, which could be assigned to the C–O–C bond, indicating the successful formation of ether bonds by the chemical acetalization reaction [15].

Figure 3(d) shows the Raman spectra of freeze-dried MXene, MP aerogels, and MPF aerogels. For freeze-dried MXene, the peak observed at 153 cm^{-1} is related to the in-plane vibrations of the flake as group vibration of titanium and carbon atoms, and the peaks at 418 and 614 cm^{-1} can be attributed to the in-plane vibrations of surface groups attached to titanium atoms and in-plane vibrations of carbon atoms, respectively [20]. The broad peak located at 1581 cm^{-1} can be assigned to the stretching of sp^3 carbon. It is worth noting that the peak intensity is dramatically decreased from MXene to MP and MPF aerogels due to the weakened in-plane motion of Ti and C atoms compared to the bare MXene nanosheet. It could be explained by the increased interfacial strength between MXene and PVA after the single and dual crosslinking reactions in MP and MPF aerogels, respectively [21].

The chemical structure of the aerogels with different crosslinking mechanisms can be further confirmed by the peak fitting of high-resolution Ti 2p and C 1s spectra for the aerogels (Figs. 3(e) and 3(f)). Compared with freeze-dried MXene, the peak areas of TiO_2 slightly increase for MP aerogel and MPF aerogel due to the possible oxidation of MXene during the heating of MP solution and MPF solution in the oven at 40 °C for 20 h [13]. For the C 1s spectra, the areas of C–C and C–O peaks of MP aerogel are dramatically increased compared with that of MXene, due to the introduction of PVA polymer by the physical crosslinking reaction. For MPF aerogel, the C–C peak area further increased after the addition of formaldehyde molecules. More importantly, a new peak located at 287.4 eV corresponding to the C–O–C bond, can be observed, demonstrating that the covalent linkage between MXene and PVA has been successfully formed through the acetalization reaction [15]. In addition, a peak located at 288.5 eV corresponding to the C=O bond is also observed, which might be attributed to the unreacted formaldehyde molecules.

3.3 Mechanical properties in water

Having captured the microstructure and composition difference of MXene-based nanocomposite aerogels, the structural stabilities in water environment of freeze-dried MXene, MP, and MPF aerogels were further investigated by exposing the aerogels to water (Fig. 4(a)). For freeze-dried MXene, the structure is decomposed within 3 min after putting the materials into water, indicating their insufficient structural stability in a liquid environment and the poor interfacial strength between MXene nanosheets without any crosslinking. For MP aerogel where MXene nanosheets are bonded with PVA polymer through hydrogen bonds, the aerogel starts to decompose after 12 h of exposure to water and is fully decomposed after 24 h upon mild shaking. The hydrogen bonds between MXene and PVA are expected to break during shaking of MP aerogel in water. Therefore, compared with the freeze-dried MXene, MP aerogel by the single crosslinking reaction is demonstrated with increased structural stability and enhanced interfacial strength; however, it is

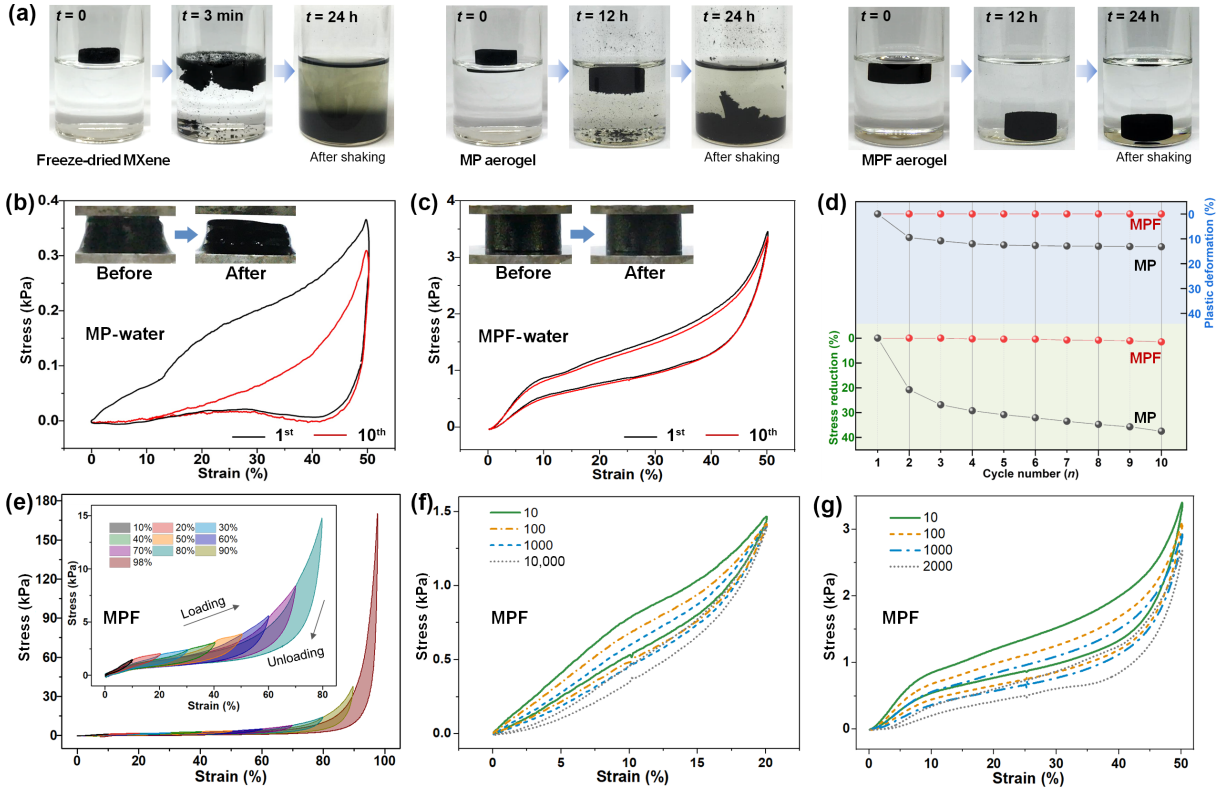

Figure 4 Structural stability and compressibility in water. (a) Photographic images showing the structural stability of the aerogels after being exposed to water. ((b) and (c)) 10-cycle stress–strain curves up to 50% compressive strain of MP aerogels (b) and MPF aerogels (c) when exposed to water; inset images show the pictures of MP and MPF aerogels before and after compression. (d) Stress reduction and plastic deformation of MP and MPF aerogels at each compressive cycle. (e) Stress–strain curves of MPF aerogels in water under different compressive strains, indicating the high compressibility of MPF aerogels. ((f) and (g)) Cyclic stress–strain curves of MPF aerogels in water at a strain level of 20% for 10,000 cycles (f) and 50% strain for 2000 cycles (g), respectively, demonstrating the outstanding mechanical durability of MPF aerogels in water.

still not robust and strong enough to conquer external stimuli even mild shaking. Impressively, MPF aerogels by the dual crosslinking mechanism can keep their cylindrical shape after being soaked for 24 h in water and even after shaking, indicating greatly enhanced structural stability in the aqueous environment. The further improved structural stability of MPF aerogels can be attributed to the ether linkages formed by the acetalization reaction during the chemical crosslinking reaction, which provides MPF aerogels with stronger interfacial strength between MXene and PVA to conquer external stimuli in water environment.

To quantitatively evaluate their structural stability and compressibility, compressive tests of MP and MPF aerogels absorbed with water up to 50% strain for 10 cycles were conducted using a universal testing machine. The test of MP aerogels with water was conducted very carefully to avoid breakage of their cylindrical shape. As shown in Fig. 4(b), MP aerogel collapsed and can not recover to its initial height after being compressed to 50% strain. The maximum stress during the 1st cycle is observed to be only 0.36 kPa, indicating the ultra-low mechanical strength of MP aerogels in aqueous environment. Surprisingly, MPF aerogel can recover to its initial height after being compressed to 50% strain for 10 cycles, showing the reversible compressibility in water (Fig. 4(c)). The maximum stress during the 1st cycle is measured to be 3.47 kPa, which is around 10 times higher than that of MP aerogels in water, clearly indicating the greatly improved mechanical strength and structural stability of MPF aerogels. In addition, MP aerogel can only maintain 62.48% of its initial stress and 86.80% of its original height, respectively at the 10th compression cycle (Fig. 4(d)). In sharp contrast, MPF aerogels show only little stress reduction (1.50%) and almost no plastic deformation (0.03%) after being compressed for 10 cycles [22]. Therefore, it can be concluded that compared to freeze-dried MXene or MP aerogels, MPF aerogels by the dual crosslinking mechanism exhibit greatly enhanced structural stability and reversible compressibility in water (see more informtaion from Movie ESM1), showing great potential for environmental applications such as wastewater treatment.

The maximum compressibility and mechanical durability of MPF aerogels in water were further tested. As shown in Fig. 4(e), the nanocomposite aerogel can recover to 100% of its original height upon unloading, even at a strain level as high as 98%, demonstrating the extremely high compressibility of MPF aerogels. As for fatigue-resistant capability test, Fig. 4(f) indicates negligible stress reduction (3.89%) and nearly no plastic deformation (0.17%) at a strain level of 20% after being compressed for 10,000 cycles. Moreover, even after being compressed for 1000 and 2000 cycles at a strain level of 50% (Fig. 4(g)), MPF aerogels can still maintain over 86.8% and 78.9% of the maximum stress, and the permanent deformations are measured to be only 0.85% and 1.67%, respectively [15, 22]. These results further prove that MPF aerogels developed by the designed dual crosslinking strategy are successfully endowed with extremely high compressibility and unprecedented mechanical durability to conquer external deformations in aqueous environment. It is worth noting that, compared to other reported MXene-based aerogels, MPF aerogels exhibit superior compressibility and fatigue resistance performance [23, 24].

3.4 Compressibility in different solvents

To further extend the application potential of MPF aerogels in organic solvents, the compressive properties of the nanocomposite aerogels up to 50% strain were systemically investigated when absorbed with different organic liquids (Figs. 5(a)–5(c) and Fig. S8 in the ESM), including polar protic solvents (ethanol), polar

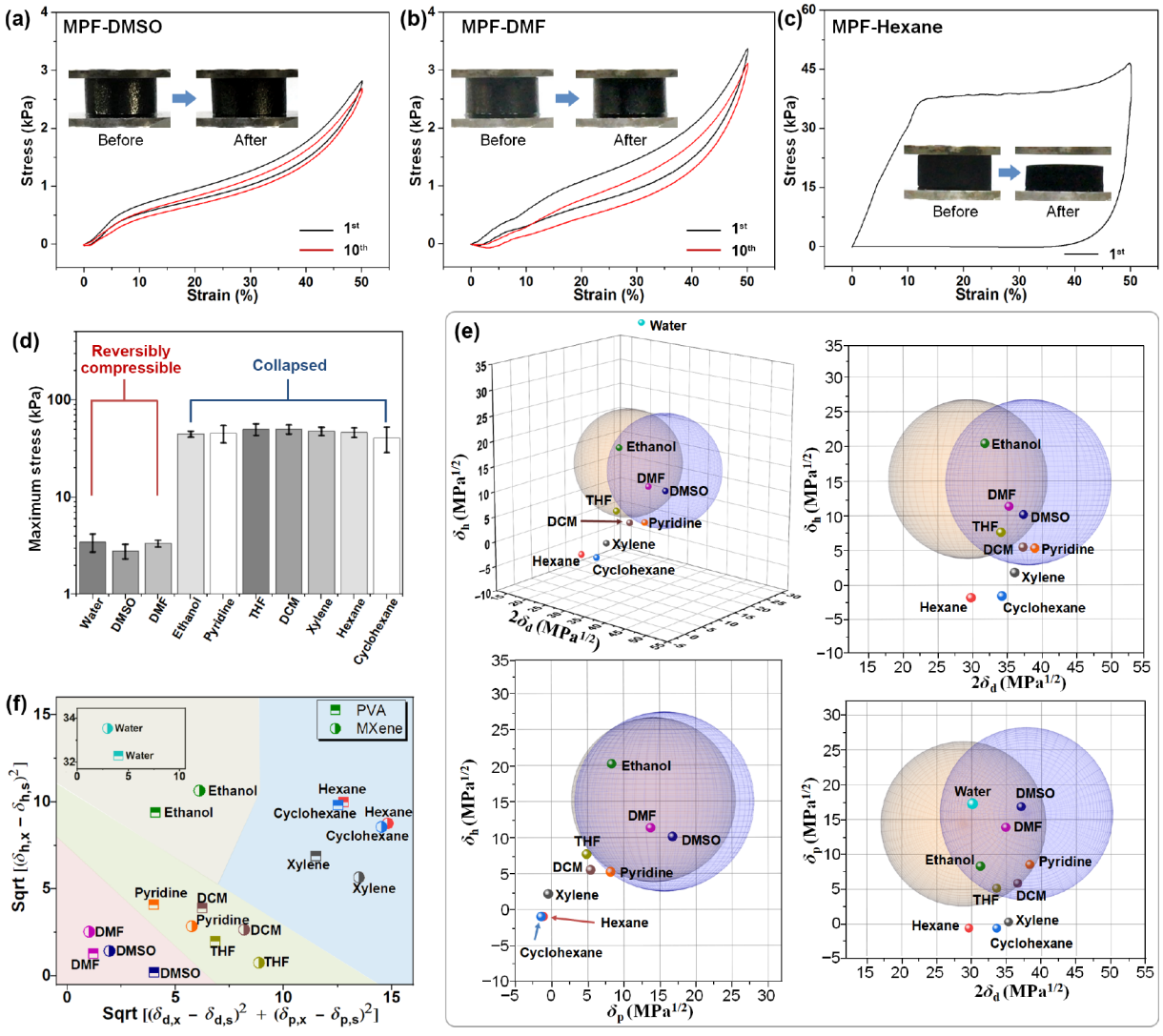

Figure 5 Compressibility of MPF aerogels in different solvents. ((a)–(c)) Stress–strain curves of MPF aerogels up to 50% compressive strain when exposed to DMSO, DMF, and hexane, respectively. (d) Maximum stress values of MPF aerogels in different solvents during 1st compressive cycle. (e) Hansen solubility sphere of MXene (purple) and PVA (orange) in different dimensions. (f) The modified 2D plot of Hansen solubility parameter difference between solute (MXene and PVA) and different solvents.

aprotic solvents (DMSO, DMF, pyridine, dichloromethane (DCM), tetrahydrofuran (THF)), and non-polar solvents (hexane, cyclohexane, and xylene). Interestingly, MPF aerogels exhibit adaptable compressibility when exposed to different solvents. Figures 5(a) and 5(b) show that MPF aerogels can recover to their initial height after being compressed up to 50% strain for 10 cycles when absorbed with DMSO and DMF, indicating reversible compressibility. The maximum stresses during the 1st cycle are 2.82 and 3.37 kPa in DMSO and DMF, respectively.

On the contrary, the compression-recovery behavior is not observed for MPF aerogels in other organic solvents, including hexane (Fig. 5(c)) and pyridine, etc. (Fig. S8 in the ESM). The aerogels are collapsed during compression and incapable of recoverability upon unloading. The maximum stresses during the 1st cycle are in the range of 40.83 to 54.15 kPa for MPF aerogels with irreversible compressibility, which is more than 10 times higher than that of MPF aerogels with reversible compressibility (Fig. 5(d)). Therefore, MPF aerogels show adaptable compressibility when exposed to different liquids. To the best of our knowledge, this is the first report about the adaptable compressibility for MXene-based aerogels.

To understand the underlying mechanism of adaptable compressive behavior of MPF aerogels in different solvents, Hansen solubility parameters (HSP) were modified and applied in this study to explain the correlation between MPF aerogels and the solvents. Materials with comparable HSP are expected to have high affinities and strong interactions with each other [25]. Total cohesion energy (E) through contributions from three types of interactions including dispersion cohesive energy (E_D), polar cohesive energy (E_P), and hydrogen bonding (E_H) [26], as described with the following Eq. (1)

$$E = E_D + E_P + E_H \quad (1)$$

Dividing this by the molar volume (V) gives the cohesion energy density ($E/V = \delta^2$)

$$\frac{E}{V} = \frac{E_D}{V} + \frac{E_P}{V} + \frac{E_H}{V} \quad (2)$$

$$\delta^2 = \delta_d^2 + \delta_p^2 + \delta_h^2 \quad (3)$$

where δ_d, δ_p, and δ_h are HSP due to the dispersion forces, dipole forces, and hydrogen bonding, respectively.

HSP of one solvent can be represented by a point in 3D space (Hansen space), where the orthogonal x-, y-, and z- axes are $2\delta_d$, δ_p, and δ_h , respectively (Fig. 5(e) and Table S2 in the ESM) [27]. For nanomaterials or polymers, the Hansen solubility sphere is used to describe the interaction of nanomaterials or polymers with different solvents, where good solvents are inside the sphere and

bad solvents are outside the sphere. The building blocks of MPF aerogels are mainly composed of MXene nanosheets (δ_d = 18.7, δ_p = 15.4, δ_h = 14.5, and R = 11) [28] and PVA polymer chains (δ_d = 14.7, δ_p = 14.1, δ_h = 14.9, and R = 10.5) [26, 27]. As shown in Fig. 5(e), the solvents located in the junction part include ethanol, DMSO, and DMF, while the other solvents remain outside the junction part of the two spheres. It should be mentioned here that water is usually seen as an outlier solvent due to its extremely high hydrogen-bonding solubility parameter [25]. The special case of ethanol might arise from the varied dispersibility and chemical structures of MXene prepared by different methods [29, 30].

To better understand the interaction between MPF aerogels and different solvents, the solubility parameter distance (R_a) was further applied [26]

$$R_a = \sqrt{4(\delta_{d,x} - \delta_{d,s})^2 + (\delta_{p,x} - \delta_{p,s})^2 + (\delta_{h,x} - \delta_{h,s})^2} \quad (4)$$

where $\delta_{d,x}$ and $\delta_{d,s}$ are HSP of solute and solvent due to dispersion force, $\delta_{p,x}$ and $\delta_{p,s}$ are HSP of solute and solvent due to dipole force, and $\delta_{h,x}$ and $\delta_{h,s}$ are HSP of solute and solvent due to hydrogen bonding. The energy of mixing in polymer solutions caused by dispersion forces and dipole forces could be integrated into the enthalpy correction parameter (χ_H) [25, 31]

$$\chi_H = \frac{V_m}{RT}\left((\delta_{d,x} - \delta_{d,s})^2 + (\delta_{p,x} - \delta_{p,s})^2\right) \quad (5)$$

where V_m is the average molar volume based on mole fraction. Together with hydrogen bond parameter δ_h, the solubility characteristics could be described in the 2D plot by using modified parameter distance $\sqrt{(\delta_{d,x} - \delta_{d,s})^2 + (\delta_{p,x} - \delta_{p,s})^2}$ and $\sqrt{(\delta_{h,x} - \delta_{h,s})^2}$ as x and y axes, respectively. The smaller x and y values represent more similar Hansen solubility parameters between the solute and solvent, thereby indicating the higher affinity and stronger interaction between the solute and solvent.

Figure 5(f) shows the calculated parameter differences of MXene (δ_d = 18.05, δ_p = 14.48, and δ_h = 8.76) [29] and PVA (δ_d = 17, δ_p = 12.1, and δ_h = 10.2) [26, 27] with different solvents. The graph can be divided into four distinct domains: the bottom left corner of polar aprotic solvents with high dielectric constant (DMSO and DMF), bottom middle of polar aprotic solvents with low dielectric constant (pyridine, DCM, and THF), top left of polar protic solvents (water and ethanol), and middle right of non-polar solvents (hexane, xylene, and cyclohexane). Interestingly, both DMSO and DMF lie in the bottom left corner with much smaller x and y values, indicating the higher affinity and stronger interaction between DMSO or DMF with MPF aerogels compared to other organic solvents. Therefore, the modified solubility parameter difference shows a high correlation between the solute–solvent interactions and the compressive behavior of MPF aerogels in all organic solvents investigated in this study. Meanwhile, it is expected that this method can also provide a guideline for predicting the mechanical response of MPF aerogels or other 2D material/polymer-based porous structures when diverse liquid environments are applied.

3.5 Adsorption testing

3.5.1 *Adsorption capacity*

Given the well-defined porous structure and reversible compressibility of MPF aerogels in an aqueous environment, the nanocomposite aerogels were investigated as recyclable cleaning adsorbents for contaminated water. As one cationic dye, methylene blue was widely investigated for adsorption studies. Therefore, taking as one example, methylene blue, was used in our study to comprehensively investigate the adsorption behavior of MPF aerogels and compare with other previously reported MXene-based absorbents. After adsorption, the equilibrium concentration of methylene blue solution (c_e) can be determined by ultraviolet–visible (UV–Vis) spectrum at the wavelength of 664 nm according to the Beer–Lambert law [19]

$$A = -\log T = \varepsilon b c_e \quad (6)$$

The adsorption capacity at equilibrium (q_e) can then be calculated based on the following equation

$$q_e = \frac{(c_0 - c_e)}{m} \times V \quad (7)$$

where c_0 is the initial concentration before adsorption, V is the volume of methylene blue solution, and m is the weight of MPF aerogels used for adsorption. Figure 6(a) shows the UV–Vis spectra and photographic images of methylene blue solution (10 mg·L^{-1}) before and after adsorption by MPF aerogel. After adsorption, the characteristic absorption peak of methylene blue at 664 nm disappeared and the solution changed from deep blue to semi-transparent, indicating the feasibility of MPF aerogels to work as an effective adsorbent for methylene blue solution. To quantitatively check the adsorption capability, the maximum adsorption capacity of MPF aerogel for methylene blue is measured by adding 20 mg of MPF aerogel into 50 mL methylene blue solution (pH 7) with an initial concentration of 200 mg·L^{-1}. After adsorption, the maximum capacity of MPF aerogel is calculated to be 117.87 mg·g^{-1}, which is dramatically increased by 1451% compared to that of PF aerogels (8.12 mg·g^{-1}) without MXene. To check the adsorption mechanism, Brunauer–Emmett–Teller (BET) specific surface area, zeta potential, and adsorption capacity of MPF aerogels and freeze-dried MXene were tested and the results are shown in Figs. S10 and S11 in the ESM. The specific surface areas of MPF aerogel and freeze-dried MXene are 7.67 and 4.32 m^2·g^{-1}, while the zeta potential values of these two are −29.80 and −40.13 mV, respectively. It is observed that the adsorption capacity of MXene-based absorbents is more affected by zeta potential, which could be possibly due to the electrostatic interaction between cationic methylene blue molecules and negatively charge MPF aerogels. For further verification, MPF aerogels were examined as adsorbents for anionic dye rose bengal. As shown in Fig. S12 in the ESM, 96.01% of methylene blue was adsorbed by MPF aerogel, while only 3.42% of rose bengal was adsorbed. Therefore, MPF aerogels with negative charge can adsorb cationic dye while anionic dye can not be adsorbed, clearly proving the electrostatic interaction as driving force for adsorption with MPF aerogels.

Recycling efficiency of adsorbents in several adsorption cycles is also an important factor. After adsorption, the porous MPF aerogels can be easily recycled and regenerated by simply squeezing out the adsorbed methylene blue in a mixed solution of NaOH and ethanol (V_1:V_2 = 1:1), followed by washing in deionized water until neutralization. Figure 6(b) shows that MPF aerogels can still maintain 89.48% and 67.72% of the maximum adsorption capacity after the 3rd and 10th adsorption cycles, respectively (pH 7, 50 mg·L^{-1}). Compared to previously reported MXene-based adsorbents, MPF aerogels are demonstrated with simultaneously high adsorption capacity and excellent recycling efficiency (Fig. 6(c) and Table S3 in the ESM). The outstanding adsorption performance of MPF aerogels can be attributed to two factors. First, the highly porous structure of MPF aerogels enhances the accessibility and transportation of methylene blue toward active sites of MPF aerogels. Second, the dual crosslinking strategy provides MPF aerogels with greatly enhanced interfacial strength and reversible compressibility, which guaranteed superior

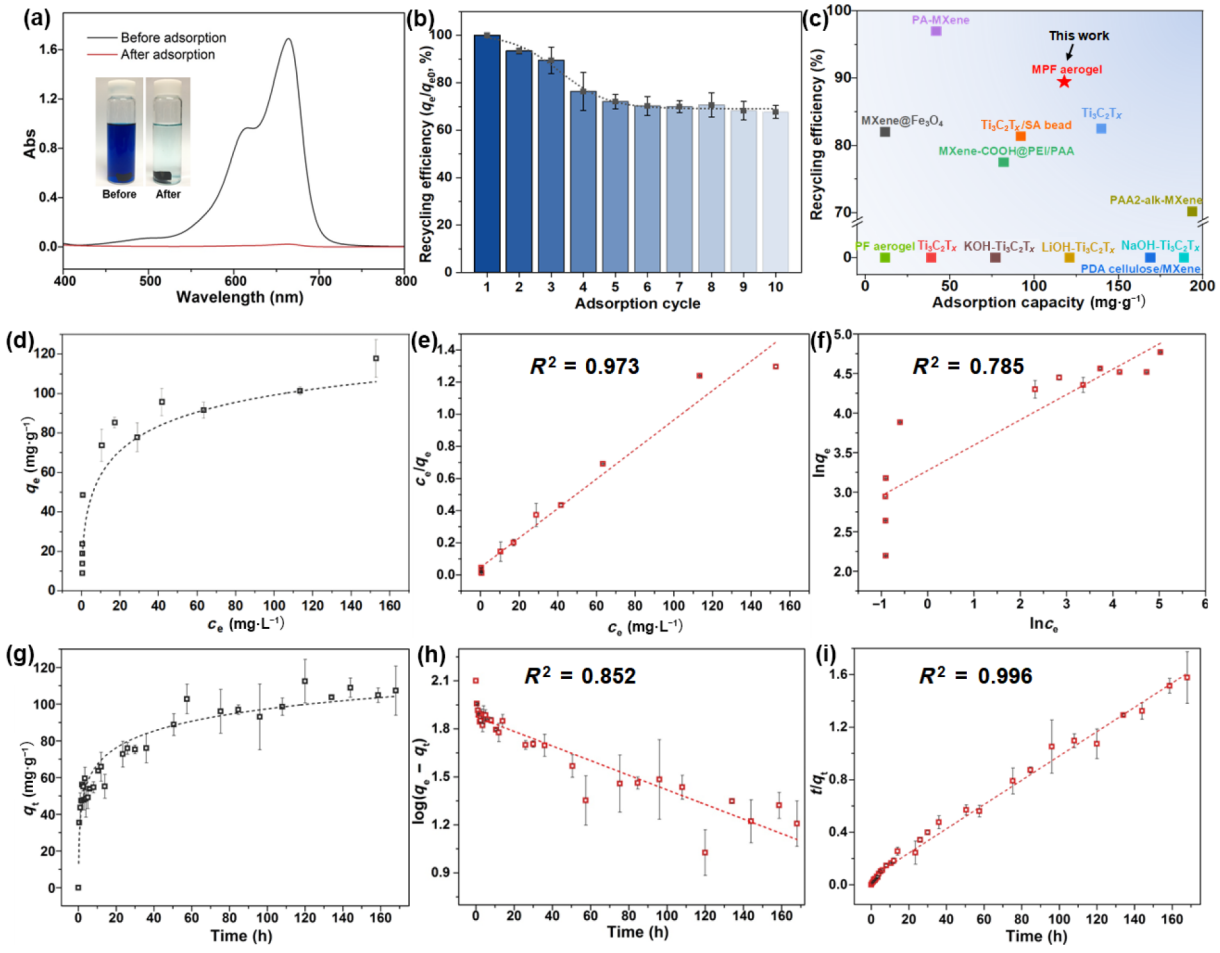

Figure 6 Methylene blue adsorption testing with MPF aerogels. (a) UV–Vis spectra and photographic images of methylene blue solution (10 mg·L^{-1}) before and after adsorption by MPF aerogels. (b) Recycling efficiencies of MPF aerogel under different adsorption cycles. (c) Comparison of adsorption capacity and recycling efficiency between MPF aerogels and previously reported MXene-based adsorbents. ((d)–(f)) Adsorption isotherm study of methylene blue by MPF aerogels (30 °C, pH 7) and the equilibrium data fitting with (d) the Langmuir isotherm model and (e) the Freundlich isotherm model, respectively. ((g)–(i)) Adsorption kinetic studies of methylene blue by MPF aerogels and the kinetic data fitting with (g) the pseudo-first-order model and (h) the pseudo-second-order model, respectively.

structural stability during the recycling process (Fig. S13 in the ESM). It is worth noting here that, except for methylene blue, MPF aerogels also show great potential as adsorbents for other cationic dyes including malachite green, methyl violet, and rhodamine B (Fig. S14 in the ESM) as well as other contaminants such as pesticides, and industrial chemicals.

3.5.2 *Adsorption isotherm study*

The adsorption isotherm was studied to analyze the adsorption phenomenon by testing the adsorption capacity at equilibrium (q_e) under different equilibrium concentration (c_e). Two isotherm models are commonly applied, the Langmuir model [32] and the Freundlich model [33], which can be expressed as follows:

Langmuir model

$$\frac{C_e}{q_e} = \frac{C_e}{q_{max}} + \frac{1}{q_{max}k_L} \quad (8)$$

Freundlich model

$$\ln q_e = \ln k_F + \frac{1}{n}\ln c_e \quad (9)$$

where q_{max} (mg·g^{-1}) is the theoretical maximum adsorption capacity and k_L is the Langmuir constant. The value of q_{max} and k_L can be calculated from the linear plot of c_e/q_e against c_e. k_F and n represent the Freundlich constant and adsorption energy distribution, respectively, which can be calculated from the linear plot of lnq_e against lnc_e. As shown in Fig. 6(d), the adsorption capacity of MPF aerogel increased from 8.99 ± 0.03 to 117.87 ± 0.59 mg·g^{-1} as the initial concentration of methylene blue solution increased from 4 to 200 mg·L^{-1}, which can be explained by the increase of the driving force caused by the increasing concentration gradient. The adsorption isotherm model can be determined based on the correlation coefficient (R^2) calculated from the linear fitting (Figs. 6(e) and 6(f) and Table S4 in the ESM). After calculation, the correlation coefficient (R^2) obtained from the Langmuir model (0.973) is estimated to be closer to 1 than that obtained from the Freundlich model (0.785). This suggests that the experimental data can be well described by the Langmuir model, indicating that the adsorption process is the monolayer adsorption taking place on a homogeneous adsorbent surface of MPF aerogels [34].

3.5.3 *Adsorption kinetic study*

The adsorption kinetic study was further conducted by examining the adsorption capacity of MPF aerogels added in methylene blue solution (initial concentration of 100 mg·L^{-1}) under different contact times. Two theoretical models, the pseudo-first-order model and pseudo-second-order model [35] were applied to fit the experimental data, which are expressed as follows:

Pseudo-first-order model

$$\log(q_e - q_t) = \log q_e - \frac{k_1}{2.303}t \quad (10)$$

Pseudo-second-order model

$$\frac{t}{q_t} = \frac{1}{k_2 q_e^2} + \frac{t}{q_e} \quad (11)$$

where q_t (mg·g^{-1}) is the adsorption capacity at a given time t (h); k_1 and k_2 are the rate constants of the pseudo-first-order and pseudo-second-order models, respectively. The adsorption capacity–time curve (Fig. 6(g)) shows that the adsorption capacity increases rapidly in the initial stage, which could be attributed to the large surface area of the porous MPF aerogel. Finally, the adsorption equilibrium was achieved with a maximum capacity of 107.31 ± 13.36 mg·g^{-1}. The linear fitting of adsorption kinetic models is shown in Figs. 6(h) and 6(i), and the calculated parameters are listed in Table S5. From the linear fitting, the correlation coefficients (R^2) of the pseudo-first-order and pseudo-second-order models are determined to be 0.852 and 0.996, respectively. Therefore, the measured kinetic data is well-fitted with the pseudo-second-order model, indicating that the adsorption rate is limited by the diffusion of methylene blue into the porous structure of MPF aerogels [19].

3.6 Thermal insulation

To demonstrate another feasible application of MPF aerogels, the thermal insulation performance of the nanocomposite aerogels was also investigated considering their highly porous structure. First, thermal conductivity of MPF aerogel was tested. Thermal conductivity (κ) can be calculated by $\kappa = \rho\alpha$Cp, where ρ is the density (26.10 mg·cm^{-3}), α is the thermal diffusivity (0.407 mm^2·s^{-1}, tested with NETZSCH LFA apparatus), Cp is the specific heat capacity (1.842 J·g^{-1}·K^{-1}, tested with differential scanning calorimeter). Thermal conductivity of MPF aerogel was calculated as 0.020 W·m^{-1}·K^{-1}, showing the low thermal conductivity. To validate the thermal insulation performance, MPF aerogels (thickness ~ 8 mm) were placed on the hotplate with constant temperatures (45, 60, 80, and 100 °C) and the surface temperatures of the aerogels were measured using a thermal infrared camera. As shown in Fig. 7(a), the top surface temperature increases with contact time. After reaching equilibrium at 30 min, the highest temperature of MPF aerogel on 100 °C hotplate was measured to be only 39.76 °C. In addition, the temperature on the side surface shows a gradient increase from the hot source to the top (Fig. 7(b)), indicating the effective thermal insulation capability of the porous MPF aerogel. Moreover, silkworm chrysalises are heated using an alcohol lamp without and with thermal insulation from MPF aerogel, respectively (Fig. 7(c)). The silkworm chrysalis without MPF aerogel protection starts to burn within 10 s. Impressively, the silkworm chrysalis on MPF aerogel can well-maintain its shape

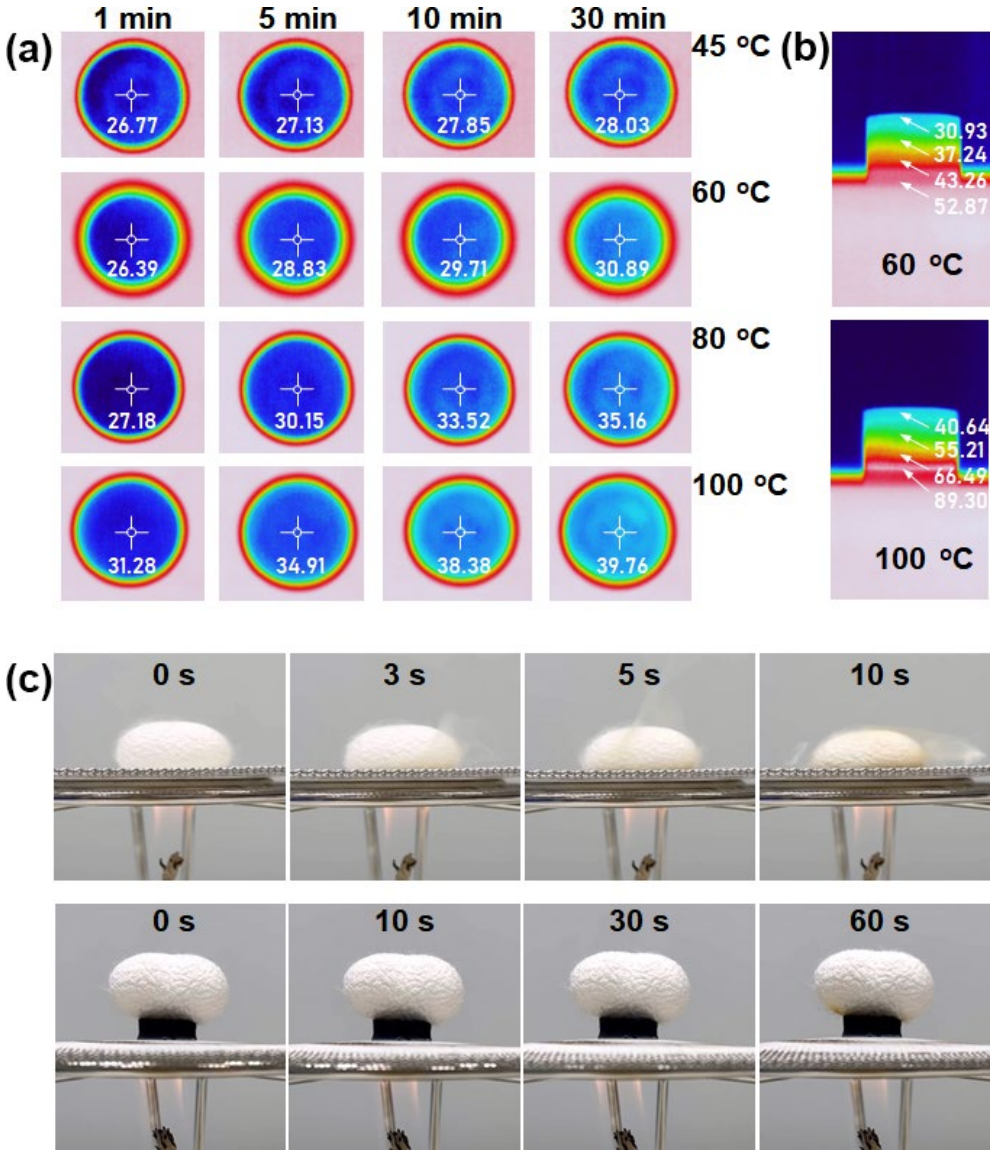

Figure 7 Thermal insulation performance of MPF aerogels. (a) Temperature changes of MPF aerogels after putting onto the hotplate with different constant temperature. (b) Surface temperature gradient of MPF aerogels after reaching equilibrium on 60 and 100 °C hotplate, respectively. (c) Photographic images of silkworm chrysalis under heating without and with the thermal protection of MPF aerogels, respectively.

with negligible change after heating for 60 s, verifying the excellent thermal resistance and thermal insulation capability of the porous MPF aerogel [13].

4 Conclusions

$Ti_3C_2T_x$ MXene-based nanocomposite aerogels were developed by the dual physical and chemical crosslinking strategy. By applying the designed interfacial engineering between MXene and PVA, the porous MPF aerogels are demonstrated with superior structural stability and extremely high compressibility up to 98% strain when absorbed with water. More impressively, MPF aerogels can still maintain their structure even after being compressed for 2000 cycles under 50% strain, implying the unprecedented mechanical durability enabled by the dual crosslinking reaction. Interestingly, the MPF aerogels exhibit adaptable compressibility with various solvents, which can be validated by the modified HSP. Taking advantage of their porous structure and high compressibility in water, MPF aerogels are observed with great promise for contaminated water treatment, by showing a high adsorption capacity for methylene blue (117.87 $mg \cdot g^{-1}$) with high recycling efficiency (89.48% at 3rd cycle). Moreover, the highly porous structure also endowed MPF aerogels with outstanding thermal insulation capability. Therefore, through the designed dual crosslinking strategy, the porous MPF nanocomposite aerogels with super elasticity and outstanding mechanical durability show great promise in a wide range of applications including environmental engineering, thermal management, wearable electronics, compressible energy storage devices, and so on.

Acknowledgements

This work was supported by the National Research Foundation of Korea (No. 2022R1A2C3011968).

Electronic Supplementary Material: Supplementary material (further details about MPF aerogels, characterization, compression test, and adsorption test) is available in the online version of this article at https://doi.org/10.1007/s12274-023-5466-8.

References

[1] Tan, C. L.; Cao, X. H.; Wu, X. J.; He, Q. Y.; Yang, J.; Zhang, X.; Chen, J. Z.; Zhao, W.; Han, S. K.; Nam, G. H. et al. Recent advances in ultrathin two-dimensional nanomaterials. *Chem. Rev.* **2017**, *117*, 6225–6331.

[2] Naguib, M.; Kurtoglu, M.; Presser, V.; Lu, J.; Niu, J. J.; Heon, M.; Hultman, L.; Gogotsi, Y.; Barsoum, M. W. Two-dimensional nanocrystals produced by exfoliation of Ti_3AlC_2. *Adv. Mater.* **2011**, *23*, 4248–4253.

[3] An, H.; Habib, T.; Shah, S.; Gao, H. L.; Radovic, M.; Green, M. J.; Lutkenhaus, J. L. Surface-agnostic highly stretchable and bendable conductive MXene multilayers. *Sci. Adv.* **2018**, *4*, eaaq0118.

[4] Liu, J.; Zhang, H. B.; Sun, R. H.; Liu, Y. F.; Liu, Z. S.; Zhou, A. G.; Yu, Z. Z. Hydrophobic, flexible, and lightweight MXene foams for high-performance electromagnetic-interference shielding. *Adv. Mater.* **2017**, *29*, 1702367.

[5] Anasori, B.; Lukatskaya, M. R.; Gogotsi, Y. 2D metal carbides and nitrides (MXenes) for energy storage. *Nat. Rev. Mater.* **2017**, *2*, 16098.

[6] Dillon, A. D.; Ghidiu, M. J.; Krick, A. L.; Griggs, J.; May, S. J.; Gogotsi, Y.; Barsoum, M. W.; Fafarman, A. T. Highly conductive optical quality solution-processed films of 2D titanium carbide. *Adv. Funct. Mater.* **2016**, *26*, 4162–4168.

[7] Ghidiu, M.; Lukatskaya, M. R.; Zhao, M. Q.; Gogotsi, Y.; Barsoum, M. W. Conductive two-dimensional titanium carbide "clay" with high volumetric capacitance. *Nature* **2014**, *516*, 78–81.

[8] Sun, Y.; Ding, R. N.; Hong, S. Y.; Lee, J.; Seo, Y. K.; Nam, J. D.; Suhr, J. MXene-xanthan nanocomposite films with layered microstructure for electromagnetic interference shielding and Joule heating. *Chem. Eng. J.* **2021**, *410*, 128348.

[9] Zhu, J. Y.; Hou, J. W.; Uliana, A.; Zhang, Y. T.; Tian, M. M.; van der Bruggen, B. The rapid emergence of two-dimensional nanomaterials for high-performance separation membranes. *J. Mater. Chem. A* **2018**, *6*, 3773–3792.

[10] Huang, K.; Li, Z. J.; Lin, J.; Han, G.; Huang, P. Two-dimensional transition metal carbides and nitrides (MXenes) for biomedical applications. *Chem. Soc. Rev.* **2018**, *47*, 5109–5124.

[11] Yun, Q. B.; Lu, Q. P.; Zhang, X.; Tan, C. L.; Zhang, H. Three-dimensional architectures constructed from transition-metal dichalcogenide nanomaterials for electrochemical energy storage and conversion. *Angew. Chem., Int. Ed.* **2018**, *57*, 626–646.

[12] Lai, J. P.; Nsabimana, A.; Luque, R.; Xu, G. B. 3D porous carbonaceous electrodes for electrocatalytic applications. *Joule* **2018**, *2*, 76–93.

[13] Liu, J.; Zhang, H. B.; Xie, X.; Yang, R.; Liu, Z. S.; Liu, Y. F.; Yu, Z. Z. Multifunctional, superelastic, and lightweight MXene/polyimide aerogels. *Small* **2018**, *14*, 1802479.

[14] Sun, Y.; Kim, M. K.; Wang, M.; Yu, J. M.; Hong, S. Y.; Nam, J. D.; Ci, L. J.; Suhr, J. Bio-inspired multiple-stimuli responsive porous materials with switchable flexibility and programmable shape morphing capability. *Carbon* **2020**, *161*, 702–711.

[15] Hong, J. Y.; Bak, B. M.; Wie, J. J.; Kong, J.; Park, H. S. Reversibly compressible, highly elastic, and durable graphene aerogels for energy storage devices under limiting conditions. *Adv. Funct. Mater.* **2015**, *25*, 1053–1062.

[16] Wan, S. J.; Li, X.; Chen, Y.; Liu, N. N.; Du, Y.; Dou, S. X.; Jiang, L.; Cheng, Q. F. High-strength scalable MXene films through bridging-induced densification. *Science* **2021**, *374*, 96–99.

[17] Lee, E.; VahidMohammadi, A.; Prorok, B. C.; Yoon, Y. S.; Beidaghi, M.; Kim, D. J. Room temperature gas sensing of two-dimensional titanium carbide (MXene). *ACS Appl. Mater. Interfaces* **2017**, *9*, 37184–37190.

[18] Xue, Q.; Zhang, H. J.; Zhu, M. S.; Pei, Z. X.; Li, H. F.; Wang, Z. F.; Huang, Y.; Huang, Y.; Deng, Q. H.; Zhou, J. et al. Photoluminescent Ti_3C_2 MXene quantum dots for multicolor cellular imaging. *Adv. Mater.* **2017**, *29*, 1604847.

[19] Sun, Y.; Chen, L.; Yu, J. M.; Yoon, B.; Lee, S. K.; Nam, J. D.; Ci, L. J.; Suhr, J. Lightweight graphene oxide-based sponges with high compressibility and durability for dye adsorption. *Carbon* **2020**, *160*, 54–63.

[20] Sarycheva, A.; Gogotsi, Y. Raman spectroscopy analysis of the structure and surface chemistry of $Ti_3C_2T_x$ MXene. *Chem. Mater.* **2020**, *32*, 3480–3488.

[21] Liu, R.; Li, W. H. High-thermal-stability and high-thermal-conductivity $Ti_3C_2T_x$ MXene/poly(vinyl alcohol) (PVA) composites. *ACS Omega* **2018**, *3*, 2609–2617.

[22] Gao, H. L.; Zhu, Y. B.; Mao, L. B.; Wang, F. C.; Luo, X. S.; Liu, Y. Y.; Lu, Y.; Pan, Z.; Ge, J.; Shen, W. et al. Super-elastic and fatigue resistant carbon material with lamellar multi-arch microstructure. *Nat. Commun.* **2016**, *7*, 12920.

[23] Liu, H.; Chen, X. Y.; Zheng, Y. J.; Zhang, D. B.; Zhao, Y.; Wang, C. F.; Pan, C. F.; Liu, C. T.; Shen, C. Y. Lightweight, superelastic, and hydrophobic polyimide nanofiber/MXene composite aerogel for wearable piezoresistive sensor and oil/water separation applications. *Adv. Funct. Mater.* **2021**, *31*, 2008006.

[24] Wang, L.; Zhang, M. Y.; Yang, B.; Tan, J. J.; Ding, X. Y. Highly compressible, thermally stable, light-weight, and robust aramid nanofibers/Ti_3AlC_2 MXene composite aerogel for sensitive pressure sensor. *ACS Nano* **2020**, *14*, 10633–10647.

[25] Chen, S. C.; Koshy, D. M.; Tsao, Y.; Pfattner, R.; Yan, X. Z.; Feng, D. W.; Bao, Z. N. Highly tunable and facile synthesis of uniform carbon flower particles. *J. Am. Chem. Soc.* **2018**, *140*, 10297–10304.

[26] Hansen, C. M. *Hansen Solubility Parameters: A User's Handbook*; 2nd ed. CRC Press: Boca Raton, 2007.

[27] Barton, A. F. M. *CRC Handbook of Solubility Parameters and Other Cohesion Parameters*; 2nd ed. Routledge: New York, 2017.

[28] Zhou, Z. Y.; Li, L.; Liu, X. Y.; Lei, H. Y.; Wang, W. J.; Yang, Y.

Y.; Wang, J. F.; Cao, Y. X. An efficient water-assisted liquid exfoliation of layered MXene ($Ti_3C_2T_x$) by rationally matching Hansen solubility parameter and surface tension. *J. Mol. Liq.* **2021**, *324*, 115116.

[29] Zhang, Q. X.; Lai, H. R.; Fan, R. Z.; Ji, P. Y.; Fu, X. L.; Li, H. High concentration of $Ti_3C_2T_x$ MXene in organic solvent. *ACS Nano* **2021**, *15*, 5249–5262.

[30] Maleski, K.; Mochalin, V. N.; Gogotsi, Y. Dispersions of two-dimensional titanium carbide MXene in organic solvents. *Chem. Mater.* **2017**, *29*, 1632–1640.

[31] Koenhen, D. M.; Smolders, C. A. The determination of solubility parameters of solvents and polymers by means of correlations with other physical quantities. *J. Appl. Polym. Sci.* **1975**, *19*, 1163–1179.

[32] Langmuir, I. The adsorption of gases on plane surfaces of glass, mica and platinum. *J. Am. Chem. Soc.* **1918**, *40*, 1361–1403.

[33] Freundlich, H. M. F. Uber die adsorption in losungen, *Z. Phys. Chem. Leipzig* **1906**, *57*, 385–470.

[34] Fan, L. L.; Luo, C. N.; Li, X. J.; Lu, F. G.; Qiu, H. M.; Sun, M. Fabrication of novel magnetic chitosan grafted with graphene oxide to enhance adsorption properties for methyl blue. *J. Hazard. Mater.* **2012**, *215–216*, 272–279.

[35] Doğan, M.; Alkan, M.; Demirbaş, Ö.; Özdemir, Y.; Özmetin, C. Adsorption kinetics of maxilon blue GRL onto sepiolite from aqueous solutions. *Chem. Eng. J.* **2006**, *124*, 89–101.